Aerospace Science and Technology 79 (2018) 255–265

Contents lists available at ScienceDirect

Aerospace Science and Technology

www.elsevier.com/locate/aescte

Optimum distributed wing shaping and control loads for highly flexible aircraft

Jared R. Hammerton [a], Weihua Su [a,*], Guoming Zhu [b], Sean Shan-Min Swei [c]

[a] Department of Aerospace Engineering and Mechanics, University of Alabama, Tuscaloosa, AL, 35487-0280, United States
[b] Department of Mechanical Engineering, Michigan State University, East Lansing, MI 48824, United States
[c] Intelligent Systems Division, NASA Ames Research Center, Moffett Field, CA, 94035, United States

ARTICLE INFO

Article history:
Received 6 October 2017
Received in revised form 25 April 2018
Accepted 24 May 2018
Available online 28 May 2018

Keywords:
Wing shaping control
Optimum wing geometry
Distributed control load
Highly flexible aircraft

ABSTRACT

In highly flexible aircraft, the large structural slenderness associated to their high-aspect-ratio wings, while bringing challenges to the design, analysis, and control of such aircraft, can be pro-actively exploited for improving their flight performance, resulting in mission-adaptive morphing configurations. This paper studies the optimum wing bending and torsion deformation of highly flexible aircraft, with distributed control loads along the wing span to achieve the optimum wing geometry. With the goal of improving flight performance across the entire flight regime, a modal based wing shaping optimization is carried out, subject to the requirement of trim and control cost limitation. While a single objective of the minimum drag can be used to find the optimum wing geometry, this paper further considers a trade-off between flight efficiency and structural integrity. In this trade-off study, a multi-objective optimization is formulated and performed, targeting for both minimizing the drag to improve flight efficiency and reducing the gust-induced wing bending moment to enhance the structural integrity. Finally, this paper explores the minimum control cost for different targets of combined flight efficiency and structural integrity. This paper provides not only an efficient way to search for the desired wing planform geometry at a given flight condition but also insights of the required control effort that is necessary to maintain the wing geometry.

1. Introduction

The improvement of aircraft operation efficiency needs to be considered over the whole flight plan, instead of a single point in the flight envelope, since the flight condition varies in a flight mission. Therefore, it is natural to employ morphing wing designs so that the aircraft can be made adaptive to different flight conditions and missions. At the advent of recent development in advanced composites as well as sensor and actuator technologies, in-flight adaptive wing/airfoil morphing is now becoming a tangible goal. Traditionally, discrete control surfaces were used to re-distribute the aerodynamic loads along the wing span during the flight, to tailor the aircraft performance. However, the deflection of discrete control surfaces may increase the aerodynamic drag. A practical alternative is to introduce conformal wing/airfoil shape changes for the aerodynamic load control. In addition, the flexibility associated with the morphing wing structures may be pro-actively utilized to improve the aircraft performance. The active aeroelastic tailoring techniques will allow aircraft designers to take advantage of the wing flexibility to create the desired wing load distribution according to the mission requirement, to improve overall aircraft operating efficiency and performance, without using the traditional discrete control surfaces. The utilization of these concepts is predicated upon the optimum shape being known and a control system which can produce this wing shape.

The question of determining the optimum wing shape has been studied in depth. Recently, Chen et al. [1] investigated the effects of various trim conditions on the aerodynamic shape optimization of the Common Research Model wing-body-tail configuration. Using a free-form distribution for the wing geometry coupled with a RANS solver for the aerodynamics, they studied the impact of a trim constraint on the optimization process. Through a series of optimizations utilizing the trim conditions at varying points in the design process, they concluded that considering the trim during optimization yields the best performance. In a similar study, Lyu and Martins [2] performed an aerodynamic optimization of the trailing edge of a wing. Their optimization showed the drag reductions (including induced drag, friction drag and wave drag of a full aircraft planform) with shape optimization of either the entire wing or just the trailing edge. Previtali et al. [3] used a concurrent

* Corresponding author.
E-mail address: suw@eng.ua.edu (W. Su).

https://doi.org/10.1016/j.ast.2018.05.045
1270-9638/

Nomenclature

a	Centrifugal acceleration ..... m/s^2
B	Body-fixed frame
b_c	semi-chord of airfoil ..... m
$\mathbf{B}^F$, $\mathbf{B}^M$, $\mathbf{N}^g$	Influence matrices for aerodynamic force, moment, and gravity force
$\bar{\mathbf{B}}_F$, $\bar{\mathbf{B}}_B$	Components of influence matrix for $\mathbf{u}$
$\mathbf{B}_u^f$, $\mathbf{B}_u^m$	Influence matrices in control loads
$\mathbf{C}_{FF}$, $\mathbf{C}_{FB}$, $\mathbf{C}_{BF}$, $\mathbf{C}_{BB}$	Components of generalized damping matrix
$\mathbf{C}^{GB}$	Rotation matrix from body frame to global frame
C_1, C_2, C_3, C_4	Optimization constraints
d	distance of midchord in front of beam reference axis ..... m
E_{max}, R_{max}	Maximum endurance and range of aircraft .... s, m
$\mathbf{F}^a$, $\mathbf{M}^a$	Aerodynamic force and moment on wing sections ..... N, N·m
$\mathbf{F}_u^{pt}$, $\mathbf{M}_u^{pt}$	Complete points loads due to $\mathbf{u}$
$\mathbf{F}_1$, $\mathbf{F}_2$, $\mathbf{F}_3$	Matrices for inflow states differential equitation
G	Global or inertial frame
$\mathbf{g}$	Gravitational acceleration vector ..... m/s^2
$\mathbf{J}$	Jacobian matrices relating independent and dependent variables
$\mathbf{K}_{FF}$	Generalized stiffness matrix
L, D, W	Total lift, drag, and weight of aircraft ..... N
l_{mc}, m_{mc}, d_{mc}	Aerodynamic lift, moment, and drag in local aerodynamic frame about midchord ..... N/m
$\mathbf{M}_{FF}$, $\mathbf{M}_{FB}$, $\mathbf{M}_{BF}$, $\mathbf{M}_{BB}$	Components of generalized inertia matrix
M_y^g	Gust-induced aerodynamic bending moment .... N·m
$\mathbf{P}_B$	Inertial rigid-body position of aircraft ..... m
$\mathbf{Q}$	Tuning matrix for control cost
$\mathbf{q}$	Trim or design variables
R	Radius of turning path ..... m
$\mathbf{R}_F$, $\mathbf{R}_B$	Flexible and rigid-body components of generalized load vector
$\mathbf{R}_F^u$, $\mathbf{R}_B^u$	Generalized loads due to $\mathbf{u}$
$\mathbf{r}_F$, $\mathbf{r}_B$	Residuals of equilibrium equation
$\mathbf{T}$	Thrust force vector ..... N
U_c	Control cost
U_∞	Flight speed ..... m/s
$\mathbf{u}$	Distributed wing shaping control force vector
w	Wing node-fixed local frame
w_g	Gust velocity ..... m/s
$\dot{y}$, $\dot{z}$, $\ddot{z}$, $\dot{\alpha}$, $\ddot{\alpha}$	Airfoil motion variables in local aerodynamic frame
α_B	Aircraft pitching angle ..... rad
α_g	Gust-induced angle of attack ..... rad
$\boldsymbol{\beta}$	Rigid-body velocity of aircraft ..... m/s, rad/s
$\boldsymbol{\varepsilon}$	Complete strain vector of aircraft
$\boldsymbol{\varepsilon}^0$	Initial strain of aircraft
$\boldsymbol{\varepsilon}_e$ (ε_x, κ_x, κ_y, κ_z)	Elemental strain vector and its components
$\boldsymbol{\zeta}$	Quaternion
η	Magnitude of mode shapes
$\boldsymbol{\lambda}$	Inflow states for unsteady aerodynamics
λ_0	Induced velocity due to wake ..... m/s
ξ_1, ξ_2	Tuning parameters in multi-objective optimizations
ρ_∞	Air density ..... kg/m^3
$\boldsymbol{\Phi}$	Linear mode shape of aircraft
φ_B	Aircraft bank angle ..... rad

approach to optimize a 3-D morphing wing. In this work, rolling moment, weight, and maneuver aerodynamic drag were considered at different flight speeds, where the wing performances were compared with those of a conventional wing. Taking the optimization a step further requires the development of a realistic system capable of producing the optimum shape that is suitable for a given flight condition. This concept was highlighted in Nguyen et al. [4], where the design of the Variable Camber Continuous Trailing Edge Flap (VCCTEF) is introduced. In addition, an optimization is performed to determine the deflection angles required throughout the trailing edge to improve the flight performance.

Many wing morphing technologies have been developed over the years as the materials and fabrication methodologies have advanced. Molinari et al. [5] presented wind tunnel and flight tests of a morphing wing built by using compliant mechanisms and piezoelectric actuators. In Nguyen et al. [6] the principles of aerodynamic shape optimization and morphing wing structures were explored. The optimization process led to the development of the VCCTEF, which was a novel concept for improving aircraft performance by drag reduction. A further study of the VCCTEF wing model was conducted by Nguyen and Ting [7], where they performed a flutter analysis of the mission-adaptive wing. The methodology included a vortex-lattice aerodynamic model coupled with a finite element structural dynamic model. Urnes et al. [8] provided an updated review of the development, design, and testing of the VCCTEF project. Under the support of the U.S. Air Force Research Laboratory, FlexSys, Inc. developed the Mission Adaptive Compliant Wing (MAC-Wing) to test and evaluate its performance. The adaptive trailing edge flap technology was combined with a natural laminar flow airfoil and tested on the Scaled Composites White Knight aircraft. The testing suggested fuel saving, weight reduction, and improved control authority [9,10]. In an effort to move from an adaptable trailing edge to a completely adaptable wing structure, the Cellular Composite Active Twist Wing was designed and tested in Cramer et al. [11], showing promising results. A scaled airplane model was built, which incorporated active twist wings and was compared to a similar rigid model with traditional control surfaces in wind tunnel tests. The active twist wings showed similar capabilities for symmetric and asymmetric movements as well as added benefits in the stall mitigation. An overview of the process used to design the composite lattice-based cellular structures for active wing shaping was presented in Jenett et al. [12], in which they presented a detailed approach for designing a low density and highly compliant structure.

Although both the optimization process and the morphing technology have improved, there is a need for a complete system, in which a robust controller may actuate and maintain the wing members to the desired optimum shape throughout the flight envelope. The controller may also perform the required maneuver and vibration control during the flight. Most current optimization schemes utilize a CFD aerodynamic model coupled with discrete structural points as design variables. These methods produce promising results. However, when optimization is performed over an entire flight plan, this approach could be very time-consuming. Moreover, these methods consider the detailed wing shape rather than the wing bending and torsions associated with highly flexible, large aspect-ratio wing members. Recent developments of morphing technologies such as the Cellular Composite Active Twist Wing take advantage of the flexible nature of high-aspect-ratio wings. Therefore, it is natural to develop an optimization scheme that mainly considers the bending and torsion of the high-aspect-ratio wings of high-altitude, long-endurance aircraft. This concept was implemented in Su et al. [13], which utilized a modal based optimization approach in determining the best feasible wing shape

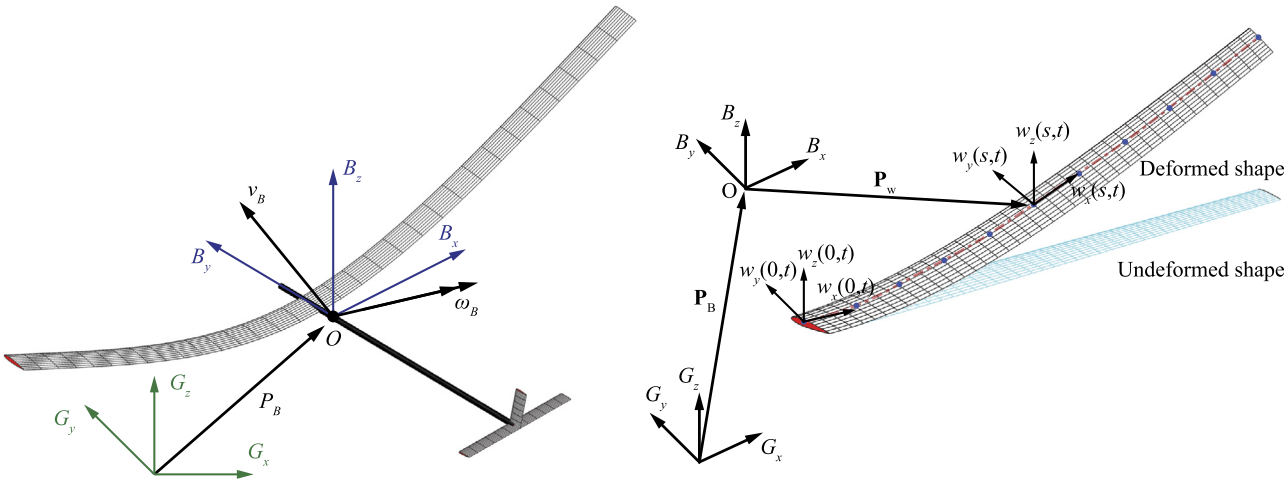

Fig. 1. Global and body frames defining the rigid-body motion of aircraft and flexible lifting-surface frames within body frame.

of a highly flexible aircraft at any given flight scenario. However, a significant disadvantage was that the distributed control loads required to actuate and maintain the optimum wing geometry were not defined. Therefore, in this paper, the study will be advanced to develop a wing optimum shape determination algorithm with defined distributed control loads. The optimization process will generate the specific wing shape needed to guarantee the optimum performance and structural integrity over the entire flight envelope of an aircraft.

2. Theoretical formulation

A coupled aeroelastic and flight dynamic formulation for highly flexible aircraft has been developed by Su and Cesnik [14–16]. A brief introduction of the formulation is presented here, followed by the modal-based optimization approach for searching the most efficient wing geometries with the optimum distributed control scheme along the wing span under different flight conditions.

2.1. Equations of motion

As shown in Fig. 1, a global or inertial frame G is defined. A body frame $B(t)$ is used to describe the vehicle position and orientation, with B_x pointing to the right and B_y pointing to the nose. The location of B is arbitrary, as long as it is in the symmetric plane of the aircraft. By taking advantage of their geometry, highly flexible wings are modeled as slender beams that may exhibit large deformations during operation. Within the body frame, a local beam frame w is designated at each node along the reference line, see Fig. 1, which is used to define the nodal position and orientation of the flexible members. In Su and Cesnik [17], a nonlinear beam element has been introduced to model the geometrically-nonlinear deformation of slender beams. In this formulation, strain deformations (curvatures) of the beam reference line are considered as the independent variables to describe the beam deformation. Assume the curvatures are constant within one element, the elemental strain vector is denoted as

$$\boldsymbol{\varepsilon}_e^T = \left\{ \varepsilon_x \quad \kappa_x \quad \kappa_y \quad \kappa_z \right\} \tag{1}$$

where ε_x is the extensional strain, κ_x, κ_y, and κ_z are the twist curvature of the beam reference line, out-of-plane bending curvature, and in-plane bending curvature, respectively. The total strain vector of the complete aircraft ε is obtained by assembling the global strain vector. Transverse shear strains are not explicitly included in this equation. However, shear strain effects are included in the constitutive relation [18]. Complex geometrically nonlinear deformations can be represented by such a constant-strain distribution over each element.

By following the Principle of Virtual Work extended to dynamic systems, the coupled aeroelastic and flight dynamic behavior of highly flexible aircraft in free flight can be described by the following equations,

$$\begin{aligned}
&\mathbf{M}_{FF}(\boldsymbol{\varepsilon})\ddot{\boldsymbol{\varepsilon}} + \mathbf{M}_{FB}(\boldsymbol{\varepsilon})\dot{\boldsymbol{\beta}} + \mathbf{C}_{FF}(\dot{\boldsymbol{\varepsilon}}, \boldsymbol{\varepsilon}, \boldsymbol{\beta})\dot{\boldsymbol{\varepsilon}} + \mathbf{C}_{FB}(\dot{\boldsymbol{\varepsilon}}, \boldsymbol{\varepsilon}, \boldsymbol{\beta})\boldsymbol{\beta} + \mathbf{K}_{FF}\boldsymbol{\varepsilon} \\
&\qquad = \mathbf{R}_F(\ddot{\boldsymbol{\varepsilon}}, \dot{\boldsymbol{\varepsilon}}, \boldsymbol{\varepsilon}, \dot{\boldsymbol{\beta}}, \boldsymbol{\beta}, \boldsymbol{\lambda}, \boldsymbol{\zeta}, \mathbf{T}, \mathbf{u}) \\
&\mathbf{M}_{BF}(\boldsymbol{\varepsilon})\ddot{\boldsymbol{\varepsilon}} + \mathbf{M}_{BB}(\boldsymbol{\varepsilon})\dot{\boldsymbol{\beta}} + \mathbf{C}_{BF}(\dot{\boldsymbol{\varepsilon}}, \boldsymbol{\varepsilon}, \boldsymbol{\beta})\dot{\boldsymbol{\varepsilon}} + \mathbf{C}_{BB}(\dot{\boldsymbol{\varepsilon}}, \boldsymbol{\varepsilon}, \boldsymbol{\beta})\boldsymbol{\beta} \\
&\qquad = \mathbf{R}_B(\ddot{\boldsymbol{\varepsilon}}, \dot{\boldsymbol{\varepsilon}}, \boldsymbol{\varepsilon}, \dot{\boldsymbol{\beta}}, \boldsymbol{\beta}, \boldsymbol{\lambda}, \boldsymbol{\zeta}, \mathbf{T}, \mathbf{u}) \\
&\dot{\boldsymbol{\zeta}} = -\frac{1}{2}\boldsymbol{\Omega}_{\zeta}(\boldsymbol{\beta})\boldsymbol{\zeta} \\
&\dot{\mathbf{P}}_B = \left[\mathbf{C}^{GB}(\boldsymbol{\zeta}) \quad \mathbf{0} \right]\boldsymbol{\beta} \\
&\dot{\boldsymbol{\lambda}} = \mathbf{F}_1 \left\{ \begin{matrix} \ddot{\boldsymbol{\varepsilon}} \\ \dot{\boldsymbol{\beta}} \end{matrix} \right\} + \mathbf{F}_2 \left\{ \begin{matrix} \dot{\boldsymbol{\varepsilon}} \\ \boldsymbol{\beta} \end{matrix} \right\} + \mathbf{F}_3\boldsymbol{\lambda}
\end{aligned} \tag{2}$$

where the components of the generalized inertia $\mathbf{M}$, damping $\mathbf{C}$, and stiffness $\mathbf{K}$ matrices can be found in [14,15]. In general, loads of aerodynamics, gravity, engine thrust, and control input are considered in the generalized load vector of aircraft, which is given as

$$\begin{aligned}
\left\{ \begin{matrix} \mathbf{R}_F \\ \mathbf{R}_B \end{matrix} \right\} = &\left\{ \begin{matrix} \mathbf{K}_{FF}\boldsymbol{\varepsilon}^0 \\ 0 \end{matrix} \right\} + \left[\begin{matrix} \mathbf{J}_{p\varepsilon}^T \\ \mathbf{J}_{pb}^T \end{matrix} \right] \mathbf{B}^F\mathbf{F}^a + \left[\begin{matrix} \mathbf{J}_{\theta\varepsilon}^T \\ \mathbf{J}_{\theta b}^T \end{matrix} \right] \mathbf{B}^M\mathbf{M}^a \\
&+ \left[\begin{matrix} \mathbf{J}_{h\varepsilon}^T \\ \mathbf{J}_{hb}^T \end{matrix} \right] \mathbf{N}^g\mathbf{g} + \left[\begin{matrix} \mathbf{J}_{p\varepsilon}^T \\ \mathbf{J}_{pb}^T \end{matrix} \right] \mathbf{T} + \left[\begin{matrix} \bar{\mathbf{B}}_F \\ \bar{\mathbf{B}}_B \end{matrix} \right] \mathbf{u}
\end{aligned} \tag{3}$$

which involves the contributions from the initial strain $\boldsymbol{\varepsilon}^0$, aerodynamic loads $\mathbf{F}^a$ and $\mathbf{M}^a$, gravitational fields $\mathbf{g}$, thrust force $\mathbf{T}$, and additional control input $\mathbf{u}$. $\mathbf{B}^F$, $\mathbf{B}^M$, and $\mathbf{N}^g$ are the influence matrices for aerodynamic lift, moment, and gravity force, respectively, which come from the numerical integration of virtual work done by the external loads along the wing span, see Su and Cesnik [14]. Influence matrices of the control input, $\bar{\mathbf{B}}_F$ and $\bar{\mathbf{B}}_B$, are dependent on the specific control mechanism and are yet to be determined in this paper. Finally, all the Jacobian matrices $\mathbf{J}$ in Eq. (3) can be obtained from the nonlinear strain-position kinematic relationship discussed in [19,17]. These Jacobian matrices link the dependent variables (the nodal positions and orientations of beam elements),

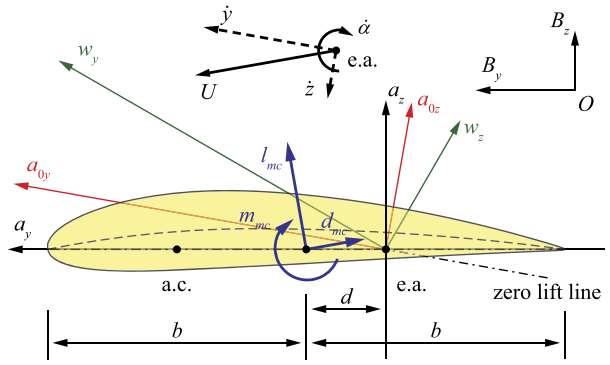

Fig. 2. Airfoil coordinate systems and velocity components.

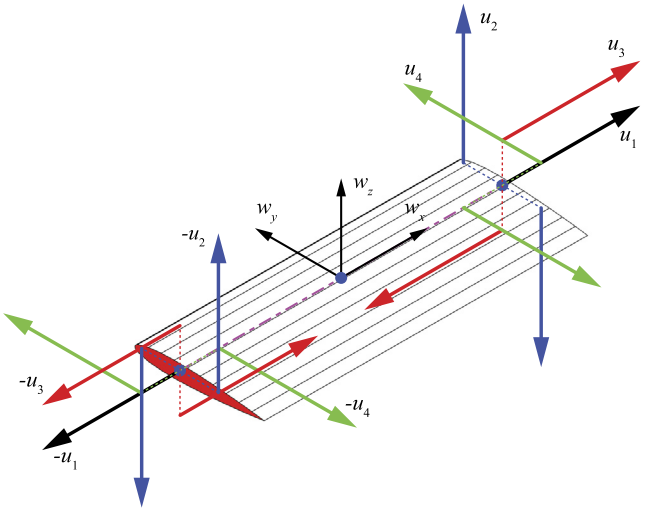

Fig. 3. Point control forces on a beam element (u_1: extension force; u_2: torsion coupling; u_3: out-of-plane bending coupling; and u_4: in-plane bending coupling).

to the independent variables (the element strain and rigid-body motion). It should be noted that both elastic member deformations and rigid-body motions are included when deriving the internal and external virtual work in Su and Cesnik [14]. Therefore, the elastic ($\boldsymbol{\varepsilon}$) and rigid-body ($\boldsymbol{\beta}$) degrees of freedom are naturally coupled. This coupling is also highlighted in Eq. (2), where the elastic deformations and the rigid-body motions are solved from the same set of equations.

In Eq. (3), aerodynamic loads are calculated by using the 2-D finite-state inflow theory [20]. At a given station along the wing, the aerodynamic lift, moment, and drag are given by

$$\begin{aligned} l_{mc} &= \pi\rho_\infty b_c^2\left(-\ddot{z}+\dot{y}\dot{\alpha}-d\ddot{\alpha}\right) \\ &\quad +2\pi\rho_\infty b_c\dot{y}^2\left[-\frac{\dot{z}}{\dot{y}}+\left(\frac{1}{2}b_c-d\right)\frac{\dot{\alpha}}{\dot{y}}-\frac{\lambda_0}{\dot{y}}\right] \\ m_{mc} &= \pi\rho_\infty b_c^2\left(-\frac{1}{8}b_c^2\ddot{\alpha}-\dot{y}\dot{z}-d\dot{y}\dot{\alpha}-\dot{y}\lambda_0\right) \\ d_{mc} &= -2\pi\rho_\infty b_c\left(\dot{z}^2+d^2\dot{\alpha}^2+\lambda_0^2+2d\dot{z}\dot{\alpha}+2\dot{z}\lambda_0+2d\dot{\alpha}\lambda_0\right) \end{aligned} \tag{4}$$

where the inflow states $\boldsymbol{\lambda}$ are governed by the inflow equation in Eq. (2). The different velocity components referred by Eq. (4) can be seen in Fig. 2. Note that the vortex-induced drag is not included in this study, as it becomes less important for the high-aspect-ratio wings studied in this paper.

2.2. Definition of general distributed control load

In the current study, a distributed control scheme is developed by assuming every element along the main wing can be actuated. Fig. 3 shows a generic wing element with applied point force (u_1) and force couples (ru_2, ru_3 and ru_4) on both ends for actuation. The combined loads may independently actuate the extensive, torsional, out-of-plane bending, and in-plane bending deformations of the element. These elemental loads are written as

$$\begin{aligned} \left(\mathbf{F}_u^{pt}\right)_e &= \left\{-u_1 \quad 0 \quad 0 \quad 0 \quad 0 \quad 0 \quad u_1 \quad 0 \quad 0\right\}^T \\ \left(\mathbf{M}_u^{pt}\right)_e &= \left\{-ru_2 \quad -ru_3 \quad -ru_4 \quad 0 \quad 0 \quad 0 \quad ru_2 \quad ru_3 \quad ru_4\right\}^T \end{aligned} \tag{5}$$

where the coefficient r represents the arms of force couples u_1, u_2, and u_3. Without loss of generality, r is set to be 1 throughout the studies. Note that there are three nodes defined on each beam element [17]. As no loads are applied at the mid-node of the element for shaping actuation, the middle three entries of both load vectors $(\mathbf{F}_u^{pt})_e$ and $(\mathbf{M}_u^{pt})_e$ are all zeros. Eq. (5) is further written into the matrix form of

$$\begin{aligned} \left(\mathbf{F}_u^{pt}\right)_e &= \begin{bmatrix} -1 & 0 & 0 & 0 & 0 & 0 & 1 & 0 & 0 \\ 0 & 0 & 0 & 0 & 0 & 0 & 0 & 0 & 0 \\ 0 & 0 & 0 & 0 & 0 & 0 & 0 & 0 & 0 \\ 0 & 0 & 0 & 0 & 0 & 0 & 0 & 0 & 0 \end{bmatrix}^T \begin{Bmatrix} u_1 \\ u_2 \\ u_3 \\ u_4 \end{Bmatrix} \\ &= \left(\mathbf{B}_u^f\right)_e \mathbf{u}_e \\ \left(\mathbf{M}_u^{pt}\right)_e &= \begin{bmatrix} 0 & 0 & 0 & 0 & 0 & 0 & 0 & 0 & 0 \\ -1 & 0 & 0 & 0 & 0 & 0 & 1 & 0 & 0 \\ 0 & -1 & 0 & 0 & 0 & 0 & 0 & 1 & 0 \\ 0 & 0 & -1 & 0 & 0 & 0 & 0 & 0 & 1 \end{bmatrix}^T \begin{Bmatrix} u_1 \\ u_2 \\ u_3 \\ u_4 \end{Bmatrix} \\ &= \left(\mathbf{B}_u^m\right)_e \mathbf{u}_e \end{aligned} \tag{6}$$

Accordingly, the complete control loads are obtained by properly sizing and assembling the elemental matrices in Eq. (6), leading to

$$\begin{aligned} \mathbf{F}_u^{pt} &= \mathbf{B}_u^f \mathbf{u} \\ \mathbf{M}_u^{pt} &= \mathbf{B}_u^m \mathbf{u} \end{aligned} \tag{7}$$

where $\mathbf{F}_u^{pt}$ and $\mathbf{M}_u^{pt}$, as nodal loads along the wing span, can be eventually transformed into the generalized control load by using the Jacobians [17], resulting in

$$\begin{Bmatrix} \mathbf{R}_F^u \\ \mathbf{R}_B^u \end{Bmatrix} = \begin{bmatrix} \mathbf{J}_{p\varepsilon}^T \\ \mathbf{J}_{pb}^T \end{bmatrix} \mathbf{B}_u^f \mathbf{u} + \begin{bmatrix} \mathbf{J}_{\theta\varepsilon}^T \\ \mathbf{J}_{\theta b}^T \end{bmatrix} \mathbf{B}_u^m \mathbf{u} = \begin{bmatrix} \bar{\mathbf{B}}_F \\ \bar{\mathbf{B}}_B \end{bmatrix} \mathbf{u} \tag{8}$$

which participated in Eq. (3) as part of the generalized load for full flexible aircraft.

2.3. Distributed control loads

Under a given flight condition, U_∞ and ρ_∞, the optimum wing geometry and control inputs should be determined to satisfy the trim of aircraft. Usually, trim variables of an airplane are

$$\mathbf{q}_{\text{trim}} = \left\{\alpha_B \quad \varphi_B \quad \mathbf{T} \quad \mathbf{u}\right\}^T \tag{9}$$

where α_B is the body pitching angle, φ_B is the bank angle, $\mathbf{T}$ is the thrust, and $\mathbf{u}$ is the control input as defined in Sec. 2.2. With the rigid-body rotation angles, α_B and/or φ_B, one can prescribe the quaternions and thus the rigid-body velocity as follows,

$$\begin{aligned}\boldsymbol{\zeta} &= \boldsymbol{\zeta}(\alpha_B, \varphi_B)\\ \boldsymbol{\beta} &= \boldsymbol{\beta}(U_\infty, \boldsymbol{\zeta})\end{aligned} \tag{10}$$

For a steady coordinated turn, the centrifugal acceleration is given by

$$a = \frac{U_\infty^2}{R} \tag{11}$$

where R is the radius of the turn path. The transformation matrix between global and body frames is determined by the pitching angle α_B and the bank angle φ_B or the quaternion $\boldsymbol{\zeta}$ as

$$\mathbf{C}^{BG} = \left(\mathbf{C}^{GB}(\boldsymbol{\zeta})\right)^T = \left(\mathbf{C}^{GB}(\alpha_B, \varphi_B)\right)^T \tag{12}$$

Therefore, the body components of the rigid-body acceleration is given by

$$\dot{\boldsymbol{\beta}} = \begin{Bmatrix} \mathbf{C}^{BG}\begin{Bmatrix} a & 0 & 0 \end{Bmatrix}^T \\ \mathbf{0}_{3\times 1} \end{Bmatrix} \tag{13}$$

Hence, the original aeroelastic and flight dynamic equations described in Eq. (2) can be simplified by considering only the prescribed rigid-body motion in terms of $\boldsymbol{\zeta}$, $\boldsymbol{\beta}$, and $\dot{\boldsymbol{\beta}}$. In addition, the transient vibration terms of the aircraft, damping effects, and unsteady aerodynamic contributions are all removed from Eq. (2), yielding

$$\begin{aligned}\mathbf{M}_{FB}(\boldsymbol{\varepsilon})\dot{\boldsymbol{\beta}} + \mathbf{K}_{FF}\varepsilon - \mathbf{R}_F(\alpha_B, \varphi_B, \mathbf{T}, \mathbf{u}, \boldsymbol{\varepsilon}) &= \mathbf{0}\\ \mathbf{M}_{BB}(\boldsymbol{\varepsilon})\dot{\boldsymbol{\beta}} - \mathbf{R}_B(\alpha_B, \varphi_B, \mathbf{T}, \mathbf{u}, \boldsymbol{\varepsilon}) &= \mathbf{0}\end{aligned} \tag{14}$$

where the generalized loads are explicitly determined by the trim variables, as well as the wing shape. Even though the flight speed U_∞, air density ρ_∞, and centrifugal acceleration a do impact the aerodynamic load, they are omitted from Eq. (14), as they are prescribed flight conditions and do not belong to the trim variables. It is clear that the second equation in Eq. (14) is essentially the trim condition that an aircraft in steady flight should satisfy, while the first is the elastic equilibrium for flexible aircraft.

In Su et al. [13], a modal based approach was presented to search for the optimum wing geometry without using the traditional control surfaces. This approach is still utilized here. Assume a wing geometry satisfying the trim condition be represented by a truncated series of linear mode shapes, i.e.,

$$\bar{\boldsymbol{\varepsilon}}(s,t) = \sum_{i=1}^{N} \boldsymbol{\Phi}_i(s)\eta_i(t) \tag{15}$$

where $\boldsymbol{\Phi}_i$ are the linear mode shapes of the flexible aircraft and η_i the corresponding magnitude of the modes. This approach allows one to use a finite number of flexible modes to search for the optimum wing shape for minimum drag while maintaining the trim and elastic equilibrium of the aircraft. Replace $\boldsymbol{\varepsilon}$ in Eq. (14) by $\bar{\boldsymbol{\varepsilon}}$, one can further write the residual equations as

$$\begin{aligned}\mathbf{r}_F &= \mathbf{M}_{FB}(\bar{\boldsymbol{\varepsilon}})\dot{\boldsymbol{\beta}} + \mathbf{K}_{FF}\bar{\boldsymbol{\varepsilon}} - \mathbf{R}_F(\alpha_B, \varphi_B, \mathbf{T}, \mathbf{u}, \eta_1, \eta_2, \cdots, \eta_N)\\ \mathbf{r}_B &= \mathbf{M}_{BB}(\bar{\boldsymbol{\varepsilon}})\dot{\boldsymbol{\beta}} - \mathbf{R}_B(\alpha_B, \varphi_B, \mathbf{T}, \mathbf{u}, \eta_1, \eta_2, \cdots, \eta_N)\end{aligned} \tag{16}$$

where the control force $\mathbf{u}$ is explicitly solved by enforcing $\mathbf{r}_F = 0$ during each iteration of the optimization process. In combination with Eq. (3), the control force is then given by

$$\begin{aligned}\mathbf{u} = \bar{\mathbf{B}}_F^{-1}\big(&\mathbf{M}_{FB}(\bar{\boldsymbol{\varepsilon}})\dot{\boldsymbol{\beta}} + \mathbf{K}_{FF}\bar{\boldsymbol{\varepsilon}}\\ &- \mathbf{K}_{FF}\boldsymbol{\varepsilon}^{\mathbf{0}} - \mathbf{J}_{p\varepsilon}^T\mathbf{B}^F\mathbf{F}^a - \mathbf{J}_{\theta\varepsilon}^T\mathbf{B}^M\mathbf{M}^a - \mathbf{J}_{h\varepsilon}^T\mathbf{N}^g\mathbf{g} - \mathbf{J}_{p\varepsilon}^T\mathbf{T}\big)\end{aligned} \tag{17}$$

This is the fully distributed control load along the wing span to actuate and maintain the desired wing geometry from the optimization solution.

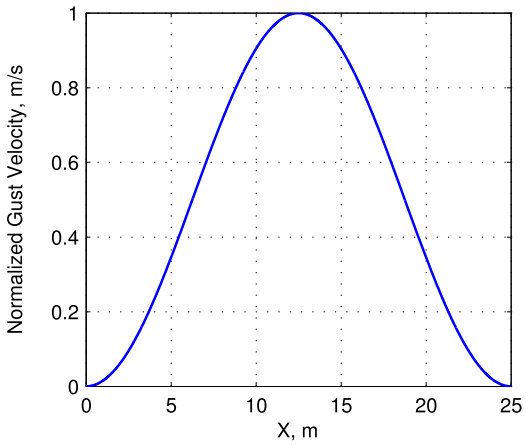

Fig. 4. A 1-cosine vertical gust velocity profile with unit peak velocity.

2.4. Multi-objective design optimization

From the previous discussion, it is clear that the design variables for the optimum wing shape may include

$$\mathbf{q} = \begin{Bmatrix} \alpha_B & \varphi_B & \mathbf{T} & \eta_1 & \eta_2 & \cdots & \eta_N \end{Bmatrix}^T \tag{18}$$

given that the optimum wing shape is represented by a finite number of linear modes. Since the minimum drag is associated with many important flight performance metrics, the first design objective of this study is to minimize the drag, that is

$$\min_{\mathbf{q}} D = D(\mathbf{q}) \tag{19}$$

At the same time, the corresponding control cost should be minimized to avoid the situation where an excessive control effort outweighs the benefit gain from the minimum drag. The control cost is defined as

$$U_c(\mathbf{q}) = \mathbf{u}^T(\mathbf{q})\mathbf{Q}\mathbf{u}(\mathbf{q}) \tag{20}$$

where $\mathbf{Q}$ is a user-defined weighting matrix to tune the control cost.

Highly flexible aircraft with slender wings are often susceptible to the perturbation of wind gust. To account for this situation and ensure aircraft structural integrity, one can define another design objective function to minimize the wing aerodynamic bending moment induced by gust perturbations. In doing so, a discrete gust model, shown in Fig. 4, is used to calculate the aerodynamic moment generated at the wing root. The gust width is 25 times the chord length of the main wing. The gust velocity can be expressed as [21]

$$w_g = \frac{w_0}{2}\left(1 - \cos\frac{2\pi x}{25c}\right) \tag{21}$$

where w_0 is the nominal maximum gust speed, and c is the average chord length of the main wing. To further simplify the problem, a method similar to Tang and Dowell [22] is used here, where the gust strength at a given time is assumed as constant along the wing span. This simplification leads to an effective angle of attack induced by the wind gust as

$$\alpha_g = \frac{w_g}{U_\infty} \tag{22}$$

with the maximum being $(\alpha_g)_{max} = w_0/U_\infty$. This additional angle of attack will be added to Eq. (4) to calculate the gust-induced aerodynamic loads. With the actual wing shape frozen, i.e., same

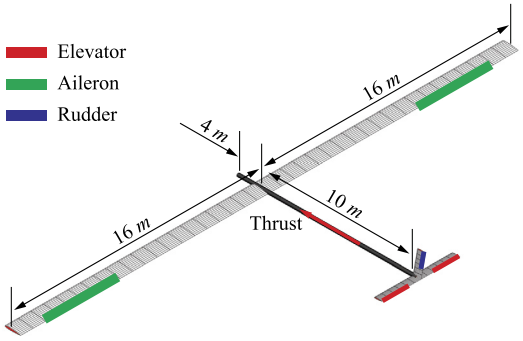

Fig. 5. Geometrical data of the baseline highly flexible aircraft.

as with no gust, the gust-induced flatwise bending moment M_y^g can be assessed at the wing root following Eq. (3), which is then to be minimized to alleviate the gust perturbation.

Finally, the optimum solution must also satisfy additional constraints. The first is the trim of aircraft, that is

$$C_1 : \mathbf{r}_B = \mathbf{0} \tag{23}$$

In addition, some variables should be constrained within their search limits, such as

$$C_2 : \begin{cases} \max|\kappa_x| \leqslant \kappa_{x\lim} \\ \max|\kappa_y| \leqslant \kappa_{y\lim} \\ \max|\kappa_z| \leqslant \kappa_{z\lim} \end{cases} \tag{24}$$

$$C_3 : \begin{cases} |\alpha_B| \leqslant \alpha_{\lim} \\ 0 \leqslant T \leqslant T_{\lim} \end{cases} \tag{25}$$

and

$$C_4 : 0 \leqslant \varphi_B \leqslant \varphi_{\lim} \tag{26}$$

To handle the proposed three design objectives, i.e., $\min D$, $\min U_c$, and $\min M_y^g$, can be a challenge. However, according to the needs for a specific flight scenario, one may choose to constrain one or two of them, while minimizing the remaining. The problem formulation and mathematical description will be given in the following numerical studies.

3. Numerical studies

In this section, a highly flexible aircraft model is considered for the numerical study. By following Su et al. [13], the vehicle's geometrical and physical properties are shown in Fig. 5 and Table 1. The aircraft has a wingspan of 32 m and a total mass of 54.5 kg. Seven linear flexible modes are used for the optimization with mode 1 being the first flat bending mode, mode 3 being the second flat bending mode, and mode 5 being the first torsion mode. A full list and description of the linear flexible modes was also provided in Su et al. [13].

3.1. Minimum drag – steady level flight

Following the approach proposed in Su et al. [13], the initial condition for design optimization is determined at first, which is achieved by trimming the aircraft using the control surfaces illustrated in Fig. 5 for a steady level flight at 20,000 m with a constant speed of 25 m/s. The resulting trimmed wing shape is shown in Fig. 6 and trim variables are used as the baseline to optimize for the minimum drag as described by Eq. (19), without applying any additional constraints. This process is then repeated, using the previous interim optimum solution as the initial condition for a new

Table 1
Properties of the baseline highly flexible aircraft.

Parameter	Value	Unit
Wings		
Span	16	m
Chord	1	m
Incidence angle	2	deg
Sweep angle	0	deg
Dihedral angle	0	deg
Beam reference axis (from LE)	50	% chord
Cross-sectional c.g. (from LE)	50	% chord
Mass per span	0.75	kg·m
Rotational moment of inertia	0.1	kg·m
Torsional rigidity	1.00×10^4	N·m^2
Flat bending rigidity	2.00×10^4	N·m^2
Edge bending rigidity	4.00×10^6	N·m^2
Tails		
Span of horizontal tail	2.5	m
Span of vertical tail	1.6	m
Chord of tails	0.5	m
Incidence of horizontal tail	−3	deg
Incidence of vertical tail	0	deg
Sweep of vertical tail	10	deg
Sweep of horizontal tail	0	deg
Dihedral of horizontal tail	0	deg
Beam reference axis (from LE)	50	% chord
Cross-sectional c.g. (from LE)	50	% chord
Mass per span	0.8	kg·m
Rotational moment of inertia	0.01	kg·m
Torsional rigidity	1.00×10^4	N·m^2
Flat bending rigidity	2.00×10^4	N·m^2
Edge bending rigidity	4.00×10^6	N·m^2
Complete aircraft		
Mass	54.5	kg

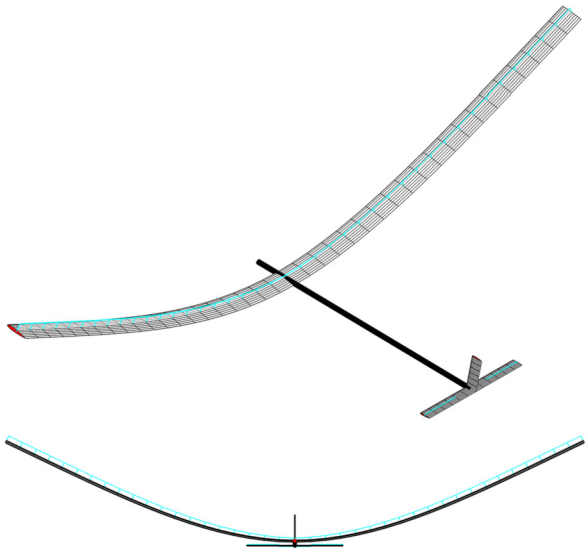

Fig. 6. Baseline trimmed geometry for steady level flight at 25 m/s.

Table 2
Minimum drag optimization results with only trim constraint.

Parameter	Baseline	Optimum
Body Angle of Attack, deg	1.26	2.62
Drag, N	59.28	51.3937
Mode 1	1.5654	0.1329
Mode 3	−0.0164	−0.0347
Mode 5	0.0071	−0.0027
Mode 7	0.0004	−0.0004
Mode 8	0.0005	−0.0013
Mode 10	−0.0002	−0.0002
Mode 12	−0.0014	−0.0013

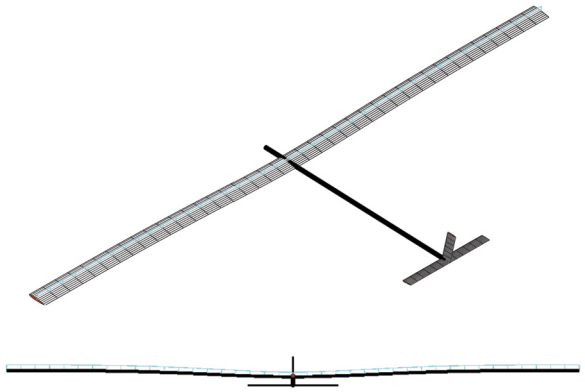

Fig. 7. Optimum geometry for steady level flight at 25 m/s.

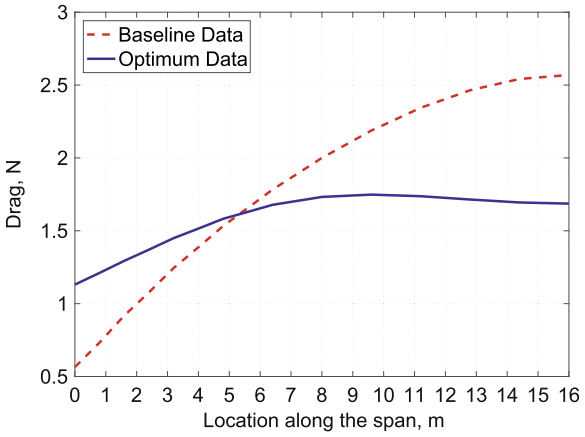

Fig. 9. Comparison of sectional drag distribution.

optimization process, until the optimum solution converges within a tolerance. During the optimization, only the symmetric modes are included. The converged solution is compared to the baseline in Table 2. The resulting optimum wing shape is shown in Fig. 7. On optimization, the optimum modal magnitudes in Table 2 results in a different wing bending and torsion distribution (see Fig. 8), which in turn changes the lift and drag distributions in the spanwise direction (see Fig. 9). In fact, the resulting optimum geometry yields a decrease in drag from 59.28 N to 51.39 N, which represents a 13.3% reduction. Table 2 also highlights the magnitude of each mode, showing that the first mode is dominant and the third mode is also significant. The higher order modes are largely unused. The optimum wing shape is mostly flat, which is consistent with the results reported in Su et al. [13]. In comparison between Figs. 6 and 7, one can observe that an amount of local lift force is generated in the lateral direction due to the wing bending deformation, which eventually is canceled on both wings. The flat optimum shape does not waste such force components since the aerodynamic force is basically in the vertical direction. Note that the total lift is identical in the two configurations. Thus, the initial shape should generate more wing sectional lift, which in turn creates more sectional drag according to Eq. (4). Therefore, the drag less with the optimum wing shape. Since this shape differs so much from the baseline "U" shape shown in Fig. 6, it is intuitive that a significant amount of control effort would be required to maintain the shape. More detailed discussions and quantitative presentations about the control cost will be provided in the following studies with a balance between flight performance and control cost.

Table 3
Minimum drag vs. control cost.

ξ_1	Drag, N	Control cost
0	53.9938	3.84×10^4
0.1	53.8530	4.02×10^4
0.2	53.8271	4.04×10^4
0.3	53.7952	4.11×10^4
0.4	53.7630	4.22×10^4
0.5	53.7014	4.53×10^4
0.6	53.5738	5.49×10^4
0.7	53.4550	6.97×10^4
0.8	53.2602	1.06×10^5
0.9	52.7555	2.92×10^5
0.92	52.5576	4.12×10^5
0.95	52.2053	7.32×10^5
0.99	51.4596	2.63×10^6
1	51.3411	3.40×10^6

3.2. Multi-objective optimization – drag and control cost

Multi-objective optimization is performed in this section to help understand the trade-off involved in improving the performance and reducing the control cost. The control cost was defined previously in Eq. (20). An objective function is then defined to consider the trade-off between the minimum drag and control cost as

$$\min_{\mathbf{q}} f = \xi_1 D + (1 - \xi_1) U_c \tag{27}$$

where $0 \leq \xi_1 \leq 1$. Varying the parameter ξ_1 results in varying the trade between minimum drag and minimum control cost. For ex-

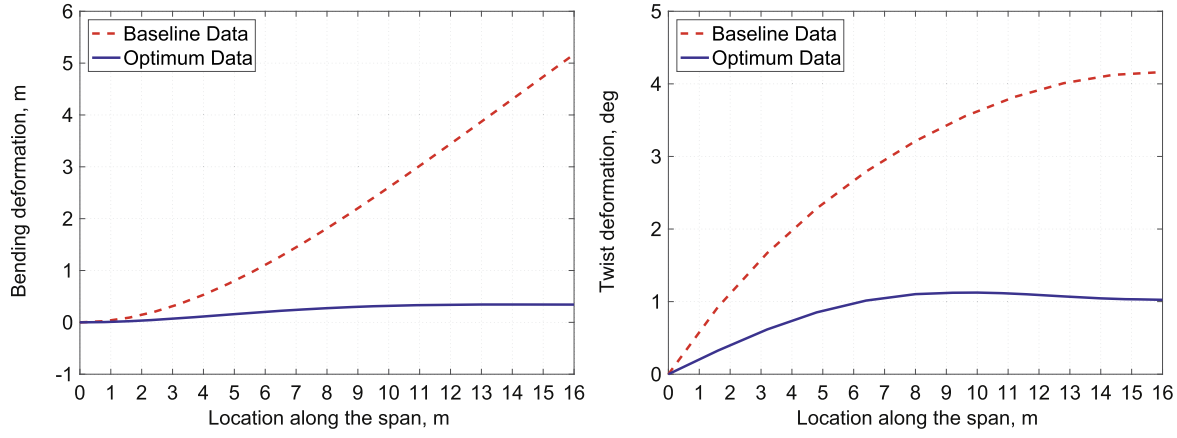

Fig. 8. Comparison of sectional bending (left) and twist (right) distributions.

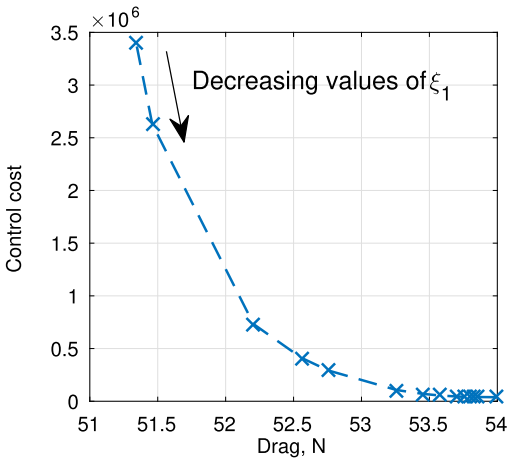

Fig. 10. Trade-off between minimum drag and control cost.

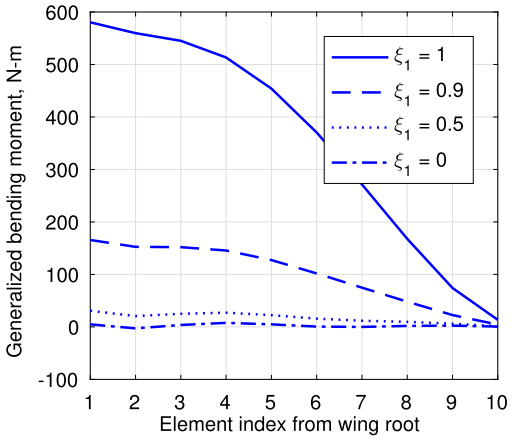

Fig. 12. Bending moment for each element of the wing for various values of ξ_1.

ample, when $\xi_1 = 1$ the objective function becomes entirely minimum drag, while $\xi_1 = 0$ becomes entirely minimum control cost. For this study, the tuning parameter is varied at an increment of 0.1. Additional cases are added for $\xi_1 = 0.92$, 0.95, and 0.99, in order to better understand the sharp change in geometry from 0.9 to 1. The results are presented in Table 3. As the parameter ξ_1 increases from 0 to 1, the minimum drag decreases with an increased control cost. This trend highlights the trade-off required between the minimum drag and the control cost. This trend can be seen graphically in Fig. 10. The optimum geometries of a few highlighted cases are presented in Fig. 11. The shape does not change dramatically between $\xi_1 = 0$ and $\xi_1 = 0.6$. After this point, the tip deflection starts to decrease more drastically. The shape transitions from a fairly deep "U" to the flat shape as seen in the minimum drag study in the previous section.

The out-of-plane bending moment required to actuate each element of the wing structure for a few highlighted values of ξ_1 are shown in Fig. 12. This figure shows the required control effort at each wing segment to achieve the appropriate geometry resulting from the corresponding optimization. It can be seen that as the parameter ξ_1 changes from 0 (minimum control cost) to 1 (minimum drag) the required bending moment in each element drastically increases, especially within the elements closer to the wing root. This observation agrees well with the shapes seen in Fig. 11, the shape becomes much flatter compared to the trim state of the aircraft, which indicates that a large bending moment is needed near the wing root to flatten the shape and thus reduce the drag.

3.3. Minimum drag with a constrained control cost

A constraint on the control cost can be used to ensure the optimum shape does not require excessive energy, while achieving drag reduction. This can be formulated as a constrained optimization problem as follows,

$$\begin{aligned} &\min_{\mathbf{q}} D = D(\mathbf{q}) \\ &\text{subject to} \quad \begin{aligned} &C_1 : \mathbf{r}_B = \mathbf{0} \\ &C_5 : U_c \leqslant U_{c\lim} \end{aligned} \end{aligned} \tag{28}$$

where $U_{c\lim}$ is a user-defined value to constrain the control cost. In this study, the limit is set at $U_{c\lim} = 7 \times 10^4$. This value corresponds to a control cost near the middle of the previous study. The resulting optimum solution is compared with the baseline in Table 4. It can be seen that the drag reduces from 59.28 N to 53.53 N, which is a 9.7% reduction. The resulting optimum geometry can be seen in Fig. 13. The shape is consistent with the ones from the previous study as it falls between $\xi_1 = 0.6$ and $\xi_1 = 0.9$,

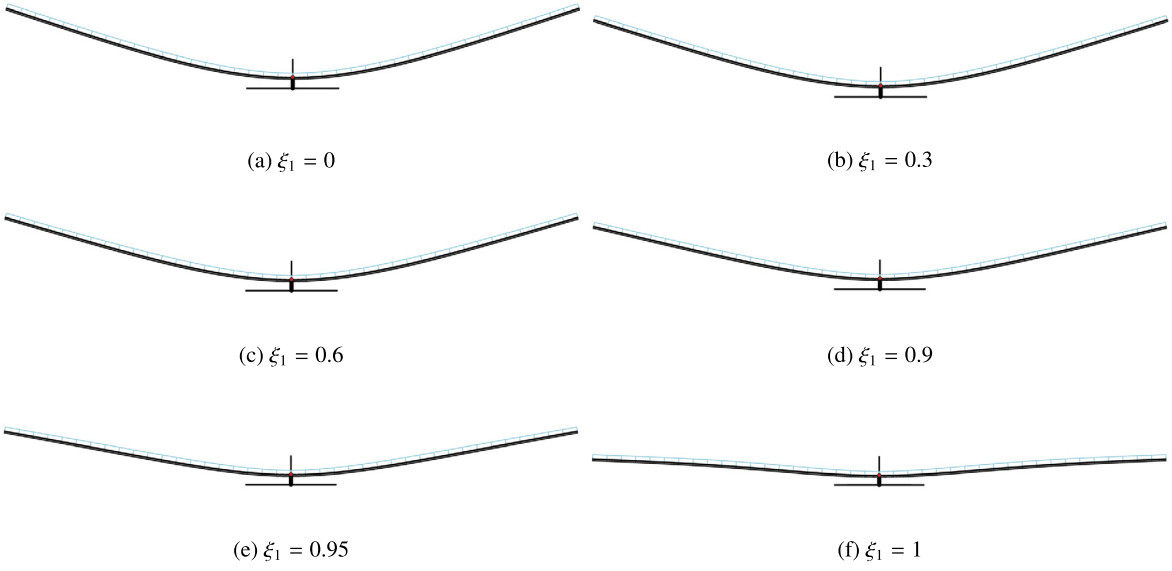

Fig. 11. Optimum geometries with trade-off between minimum drag and control cost.

Table 4
Minimum drag with control cost constraint.

Parameter	Original	Optimum
Angle of Attack, deg	1.26	2.95
Drag, N	59.28	53.53
Mode 1	1.5654	0.9962
Mode 3	−0.0164	−0.0215
Mode 5	0.0071	−0.0015
Mode 7	0.0004	−0.0002
Mode 8	0.0005	−0.0011
Mode 10	−0.0002	−0.0003
Mode 12	−0.0014	−0.0037

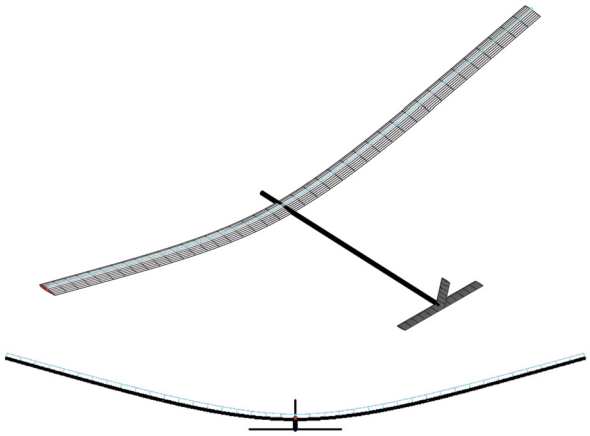

Fig. 13. Optimum geometry for steady level flight at 25 m/s with control cost constraint.

just as the control cost falls between those same weighting parameters.

3.4. Multi-objective optimization – minimum drag vs. gust load alleviation

The concept of gust alleviation discussed here is a passive way to improve the structural integrity of the aircraft under gust perturbation. The wind gust model and the approach for estimation of the gust-induced bending moment were given in Sec. 2.4. The gust velocity, w_0, is set at 2.19 m/s, which leads to an induced angle of attack of 5° for the flight speed of 25 m/s. Some aircraft missions may require this to be considered in addition to the flight performance requirements, such as drag reduction. In doing so, a different optimization is performed to better understand the potential trade-off between the flight efficiency and structural integrity by minimizing the drag and the gust-induced root bending moments. In this study, the optimization problem can be expressed as

$$\min_{\mathbf{q}} f = \xi_2 D + (1-\xi_2) M_y^g \tag{29}$$

where $0 \le \xi_2 \le 1$. The control constraint, C_5, was again set at $U_{c\text{lim}} = 7 \times 10^4$ to ensure the control cost is not too large. The parameter ξ_2 is varied at an increment of 0.1. When $\xi_2 = 0$ the optimization is entirely to find the minimum root moment, and when $\xi_2 = 1$ the optimization is entirely to find the minimum drag. The results of this study can be seen in Table 5 and graphically in Fig. 14, which very clearly show the required trade-off between flight performance and structural integrity. As a smaller drag is achieved, the wing root aerodynamic bending moment increases and vice versa.

For a battery-powered, propeller-driven aircraft, the endurance and range are given by

Table 5
Minimum drag vs. gust-induced bending moment.

ξ_2	Drag, N	M_y^g, N·m
0	55.6345	2.938×10^3
0.1	55.6115	2.938×10^3
0.2	55.6030	2.938×10^3
0.3	55.5731	2.939×10^3
0.4	55.5563	2.941×10^3
0.5	55.2553	2.959×10^3
0.6	54.1515	3.068×10^3
0.7	53.7545	3.131×10^3
0.8	53.6611	3.151×10^3
0.9	53.4783	3.219×10^3
1	53.4692	3.278×10^3

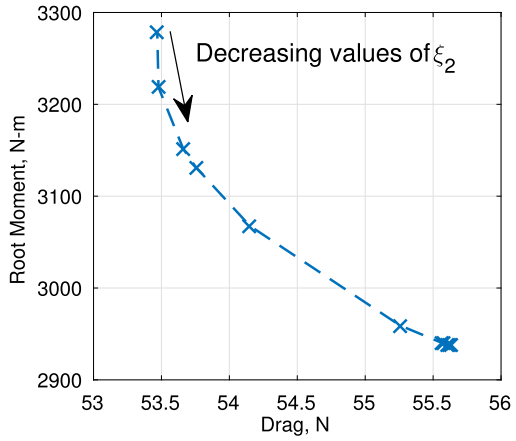

Fig. 14. Trade-off between minimum drag and gust-induced aerodynamic bending moment.

$$E = \frac{\sqrt{2}}{2} \frac{\bar{\eta} U_\infty \sqrt{\rho_\infty S}}{W^{3/2}} \frac{L^{3/2}}{D} \left(\bar{C}_0 - \bar{C}_1\right)$$
$$R = \frac{\bar{\eta} U_\infty}{W} \frac{L}{D} \left(\bar{C}_0 - \bar{C}_1\right) \tag{30}$$

where flight speed U_∞ is constant. Lift L equals weight W, both of which are time-invariant for a battery-powered aircraft under constant atmospheric conditions. ρ_∞ is the air density, S is the lifting surface area, and $\bar{\eta}$ is the propulsion efficiency. $\bar{C}_0$ and $\bar{C}_1$ are initial and final battery capacities. In fact, Eq. (30) can be derived from the Breguet Equations for range and endurance of fuel-burn propeller-driven aircraft, with assumptions of linear battery capacity discharge rate and constant aircraft weight. Nonetheless, it is clear that both endurance and range are inversely proportional to the drag D, with a constant lift at level flight. With this relationship, one can further convert Fig. 14 into the trade-off between gust-induced root bending moment and flight endurance or range, see Fig. 15. Since aircraft power capacity and propulsion efficiency are not involved in the current study, Fig. 15 is plotted with non-dimensional data, that is, all data are normalized with respect to the case when $\xi_2 = 0$. From Fig. 15, it is easy to observe the gain on the maximum endurance or range, at the cost of an increased root-bending moment.

3.5. Multi-objective optimization – minimum control with constrained drag and bending moment

To understand the trade-offs between all three quantities, drag D, gust-induced root bending moment M_y^g, and control cost U_c, a study is performed to balance the effects of all three. The root bending moment and the drag can be considered as additional constraints when performing an optimization in which the

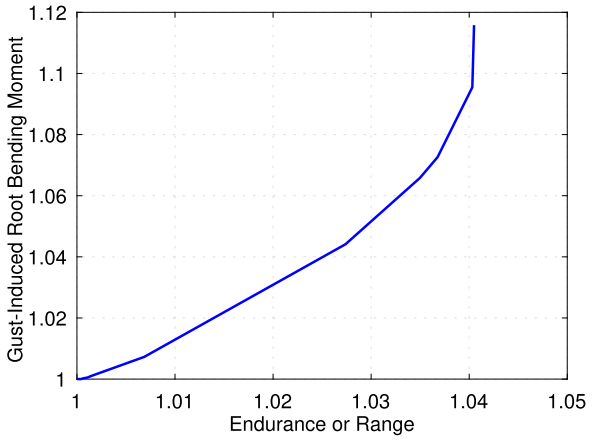

Fig. 15. Flight endurance (or range) and gust-induced root bending moment.

control cost is to be minimized. The modified optimization problem is expressed as

$$\min_{\mathbf{q}} U_c = U_c(\mathbf{q}) \tag{31}$$

subject to the following constraints

$$\begin{aligned} C_6 &: D \leqslant D_{\text{lim}} \\ C_7 &: M_y^g \leqslant M_{y_{\text{lim}}}^g \end{aligned} \tag{32}$$

In the study, one may vary the constraints of both drag and gust-induced root bending moment within a given range. With that, the minimum control cost is searched with different combinations of drag and bending moment constraints. Presented here are the results of a study in which the drag constraint is varied from 52 N to 62 N at an increment of 0.5 N, and the root bending moment constraint is varied from 2700 N·m to 3100 N·m at every 25 N·m. This study provides an aircraft designer a better understanding of the control cost required to fly an aircraft with specific constraints on the drag and root moment experienced due to gust. For illustration, a grid of drag and root moment constraints are applied to generate the plot seen in Fig. 16. It can be seen that there is a region, where the target drag and gust-induced moment are both small, therefore no feasible optimum solutions of wing geometry, and thus the control cost, exist. This infeasible region is seen in the left corner of the figure. There is a clear border where the control cost is relatively high to limit the gust moment and achieve the required wing geometry. However, the control cost is reduced when the constraints are relaxed, namely the points on the right side of the figure.

Table 6
Optimum wing geometry for a range of speeds.

Speed, m/s	Baseline		Optimum shape	
	Thrust, N	Body AOA, deg	Thrust, N	Body AOA, deg
20	87.468	4.528	85.664	4.080
21	80.110	3.699	77.251	3.694
22	73.756	2.973	69.841	3.311
23	68.245	2.333	63.634	3.141
24	63.454	1.766	58.234	3.029
25	59.282	1.260	53.541	2.941
26	55.665	0.803	49.418	2.890
27	52.521	0.389	45.816	2.874
28	49.811	0.010	43.610	2.775

3.6. Level flight in a range of speed

In this section, the wing bending and torsion geometry of the flap-less aircraft is optimized in a range of flight speed from 20 to 28 m/s, while the other sizing and geometry parameters (e.g., span and wing incidence angle) are not changed. Following the approach in Sec. 3.3, the optimization with a control cost constraint is carried out. Each of these cases is treated as an individual steady level flight case, meaning only the symmetric modes are considered as design variables. The aircraft is again trimmed using the traditional control surfaces for each flight speed to have a point of comparison with the optimum solution as well as an initial set of design variables. The optimum shapes are compared with the trim conditions for each case in Table 6. It can be seen that for each speed, the optimization produces a wing geometry that reduces the drag, thus the required thrust to maintain the trim. The size of the reduction varies with the speed range with a maximum reduction of 12.7% occurring when the speed is 27 m/s and a minimum reduction of 2.1% when the speed is 20 m/s.

4. Conclusions

Determination of the optimum wing geometry, as well as the corresponding control loads of a highly flexible aircraft, was explored in this paper. Given the flexible nature of aircraft with high-aspect-ratio wings, a modal based approach was used in determining the optimum wing bending and torsion geometry. The magnitudes of the modes were used as design variables in the optimization. Additionally, a distributed control actuation was formulated by assuming that each element of the main wing can be

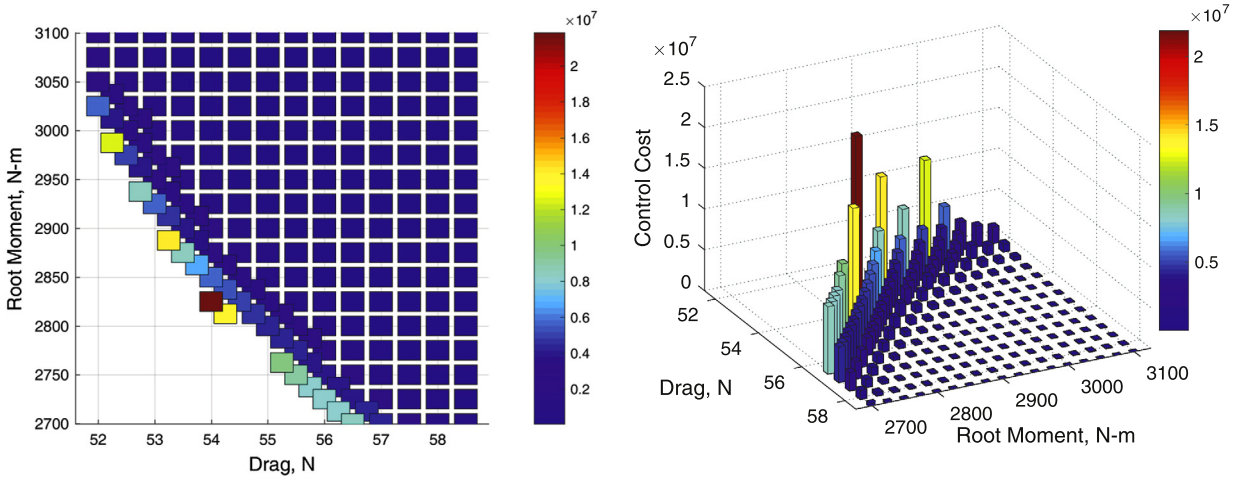

Fig. 16. Minimum control cost with varying drag and root moment constraints (left: top view; right: angle view).

actuated. This kind of modeling gave an insight into the forces and moments required to generate a specific wing geometry. The distributed force calculation was included in the optimization to determine each corresponding optimum wing geometry. In case only the trim requirement was considered in the optimization, the search for the optimum wing shape resulted in a flat wing platform, which required excessive control effort. Obviously, this excessive control cost to maintain the shape may outperform the reduction in drag. Therefore, the control cost was then included in the optimization problem formulation. A trade-off was then attained between drag reduction and control cost. The optimization was also expanded to include gust alleviation as an objective function. This multi-objective function provided insights into the trade-off between performance metrics of minimum drag and structural integrity. The control cost was also determined for different levels of flight efficiency and structural integrity, through a constrained optimization process. Aircraft designers may benefit from the study with a better understanding of the control cost required to fly an aircraft at a specific pairing of drag and root moment experienced due to gust.

It should be noted that the optimization was computed using the gradient-based optimizer *fmincon* in MATLAB, which can only produce a local minimum. Despite not being a global minimum, the results presented here were consistent and showed significant improvement over the baseline solutions.

The results presented here serve as the foundation for future works in developing the robust flight control algorithms to actuate and maintain the optimum wing geometry for any flight condition. It has been demonstrated that the optimum shape over a range of speeds appears to be a visually smooth transition. These results will be used along with linear parameter-varying modeling techniques to develop a flight controller.

Conflict of interest statement

There is no conflict of interest.

Acknowledgements

The research is supported by the Convergent Aeronautics Solutions (CAS) project of NASA ARMD. The first author also acknowledges the support of the Alabama Space Grant Consortium (ASGC) Fellowship. The views expressed in this paper are those of the authors and do not reflect the official policy or position of NASA or the U.S. Government.

References

[1] S. Chen, Z. Lyu, G.K.W. Kenway, J.R.R.A. Martins, Aerodynamic shape optimization of common research model wing-body-tail configuration, J. Aircr. 53 (1) (2016) 276–293, https://doi.org/10.2514/1.C033328.

[2] Z. Lyu, J.R.R.A. Martins, Aerodynamic shape optimization of an adaptive morphing trailing-edge wing, J. Aircr. 52 (6) (2015) 1951–1970, https://doi.org/10.2514/1.C033116.

[3] F. Previtali, A.F. Arrieta, P. Ermanni, Performance of a three-dimensional morphing wing and comparison with a conventional wing, AIAA J. 52 (10) (2014) 2101–2113, https://doi.org/10.2514/1.J052764.

[4] N. Nquyen, K. Trinh, K. Reynolds, J. Kless, M. Aftosmis, J. Urnes, C. Ippolito, Elastically shaped wing optimization and aircraft concept for improved cruise efficiency, in: 51st AIAA Aerospace Sciences Meeting Including the New Horizons Forum and Aerospace Exposition, AIAA, Grapevine, TX, 2013.

[5] G. Molinari, A.F. Arrieta, M. Guillaume, P. Ermanni, Aerostructural performance of distributed compliance morphing wings: wind tunnel and flight testing, AIAA J. 54 (12) (2016) 3859–3871, https://doi.org/10.2514/1.J055073.

[6] N. Nguyen, U. Kaul, S. Lebofsky, E. Ting, D. Chaparro, J. Urnes, Development of variable camber continuous trailing edge flap for performance adaptive aeroelastic wing, in: SAE AeroTech Congress and Exhibition, SAE, Seattle, WA, 2015.

[7] N. Nguyen, E. Ting, Flutter analysis of mission-adaptive wing with variable camber continuous trailing edge flap, in: 55th AIAA/ASME/ASCE/AHS/ASC Structures, Structural Dynamics, and Materials Conference, AIAA, National Harbor, MD, 2014.

[8] J. Urnes, N. Nguyen, C. Ippolito, J. Totah, K. Trinh, E. Ting, A mission-adaptive variable camber flap control system to optimize high lift and cruise lift-to-drag ratios of future N+3 transport aircraft, in: 51st AIAA Aerospace Sciences Meeting Including the New Horizons Forum and Aerospace Exposition, AIAA, Grapevine, TX, 2013.

[9] S. Kota, R. Osborn, G. Ervin, D. Maric, P. Flick, D. Paul, Mission adaptive compliant wing – design, fabrication and flight test mission adaptive compliant wing, in: RTO Applied Vehicle Technology Panel (AVT) Symposium, NATO, Evora, Portugal, 2016.

[10] J.A. Hetrick, R.F. Osborn, S. Kota, P.M. Flick, D.B. Paul, Flight testing of mission adaptive compliant wing, in: 48th AIAA/ASME/ASCE/AHS/ASC Structures, Structural Dynamics, and Materials Conference, AIAA, Honolulu, HI, 2007.

[11] N.B. Cramer, K. Cheung, S.S.-M. Swei, Design and testing of a lattice-based cellular component active twist wing, in: 24th AIAA/AHS Adaptive Structures Conference, AIAA, San Diego, CA, 2016.

[12] B. Jenett, S. Calisch, D. Cellucci, N. Cramer, N. Gershenfeld, S. Swei, K.C. Cheung, Digital morphing wing: active wing shaping concept using composite lattice-based cellular structures, Soft Robot. 4 (1) (2016) 33–48, https://doi.org/10.1089/soro.2016.0032.

[13] W. Su, S.S.-M. Swei, G.G. Zhu, Optimum wing shape of highly flexible morphing aircraft for improved flight performance, J. Aircr. 53 (5) (2016) 1305–1316, https://doi.org/10.2514/1.C033490.

[14] W. Su, C.E.S. Cesnik, Nonlinear aeroelasticity of a very flexible blended-wing-body aircraft, J. Aircr. 47 (5) (2010) 1539–1553, https://doi.org/10.2514/1.47317.

[15] W. Su, C.E.S. Cesnik, Dynamic response of highly flexible flying wings, AIAA J. 49 (2) (2011) 324–339, https://doi.org/10.2514/1.J050496.

[16] W. Su, C.E.S. Cesnik, Strain-based analysis for geometrically nonlinear beams: a modal approach, J. Aircr. 51 (3) (2014) 890–903, https://doi.org/10.2514/1.C032477.

[17] W. Su, C.E.S. Cesnik, Strain-based geometrically nonlinear beam formulation for modeling very flexible aircraft, Int. J. Solids Struct. 48 (16–17) (2011) 2349–2360, https://doi.org/10.1016/j.ijsolstr.2011.04.012.

[18] C.E.S. Cesnik, D.H. Hodges, Vabs: a new concept for composite rotor blade cross-sectional modeling, J. Am. Helicopter Soc. 42 (1) (1997) 27–38, https://doi.org/10.4050/JAHS.42.27.

[19] C.M. Shearer, C.E.S. Cesnik, Nonlinear flight dynamics of very flexible aircraft, J. Aircr. 44 (5) (2007) 1528–1545, https://doi.org/10.2514/1.27606.

[20] D.A. Peters, M.J. Johnson, Finite-state airloads for deformable airfoils on fixed and rotating wings, in: P.P. Friedmann, J.C.I. Chang (Eds.), Symposium on Aeroelasticity and Fluid Structure Interaction Problems, ASME Winter Annual Meeting, vol. AD – vol. 44, ASME, New York, NY, 1994, pp. 1–28.

[21] F.M. Hoblit, Gust Loads on Aircraft: Concepts and Applications, AIAA Education Series, American Institute of Aeronautics and Astronautics, Inc., Washington, DC, 1988.

[22] D. Tang, E.H. Dowell, Experimental and theoretical study of gust response for a wing-store model with freeplay, J. Sound Vib. 295 (3) (2006) 659–684, https://doi.org/10.1016/j.jsv.2006.01.024.